The Difference Between a Collapsed Cone Based and a Monte Carlo Based Dose Calculation Algorithm

VICTOR LÖF

Master of Science Thesis

TRITA FYS 2015-36
ISSN 0280-316X
ISRN KTH/FYS/–15:36—SE

KTH School of Engineering Sciences
SE-100 44 Stockholm
SWEDEN

Examiner: Mats Danielsson
Supervisor at RaySearch Laboratories: Björn Hårdemark
Supervisor at KTH: Hans Bornefalk

Abstract

In radiation therapy there is a planning process that requires simulations of dose distributions. One clinically used dose calculation algorithm for photons is called the Collapsed Cone (CC) dose algorithm. The CC dose algorithm calculates dose with known approximations such as the no kernel tilt approximation. The goal of this study was to compare the CC dose algorithm and a Monte Carlo (MC) dose algorithm in a water phantom and heterogeneous phantoms to see if potential differences could be tied to known approximations in the CC dose algorithm.

The study was divided into simulations in a water phantom and in three heterogeneous phantoms. The simulations in the water phantom studied the effects of the no kernel tilt approximation and flattening filter energy fluence spectrum. Moreover, a new CC dose algorithm including a kernel tilt implementation was evaluated against the old CC dose algorithm and the MC dose algorithm. The three heterogeneous phantoms were based on previous studies and the results were later compared with these studies.

The result from the simulations in the water phantom showed significant differences between the old CC dose algorithm and the MC dose algorithm. These differences were more pronounced for large fields both outside and inside the field. The simulation models implied the primary cause of these differences to be the no kernel tilt approximation. The new CC dose algorithm with a kernel tilt implementation showed a four times better agreement with MC dose algorithm compared to the old CC dose algorithm. The flattening filter energy fluence spectrum affected the penumbra region moderately.

The results from the simulations in heterogeneous phantoms showed that both CC dose algorithms overestimated the dose in low-density regions compared to MC dose algorithm. This was due to increased lateral scattering of electrons in low-density regions not predicted by the CC dose algorithm.

It was suggested to further develop the new CC dose algorithm to correctly include kernel tilt in the event of a new product version of the CC dose algorithm.

Sammanfattning

Planeringsprocessen vid strålterapi kräver simuleringar av dos. En av de kliniskt använda dosalgoritmerna vid planering av strålterapi med fotoner kallas för Collapsed Cone (CC) dosalgoritmen. CC-dosalgoritmen beräknar dos med kända approximationer t.ex. utan vridning av kärnan. Målet med studien var att jämföra CC-dosalgoritmen med en Monte Carlo (MC) dosalgoritm i vattenfantom och i heterogena fantom för att se om potentiella skillnader kunde knytas till kända approximationer i CC-dosalgoritmen.

Studien delades in i simuleringar i vattenfantom och i tre heterogena fantom. I vattenfantomen studerades effekterna av att inte vrida kärnan och utjämningsfiltrets energifluensspektrum. Utöver detta, implementerades en ny CC-dosalgoritm med vridna kärnor. Denna dosalgoritm utvärderades mot den gamla CC-dosalgoritmen och MC-dosalgoritmen. De tre heterogena fantomen baserades på tidigare studier och resultaten jämfördes sedan med dessa.

Resultatet från simuleringar i vattenfantomen visade på signifikanta skillnader mellan den gamla CC-dosalgoritmen och MC-dosalgoritmen. Skillnaderna var mer uttalade för stora fält både utanför och inuti fälten. Simuleringsmodellerna visade att skillnaderna troligtvis betrodde på approximationen att inte vrida kärnan. Utöver detta visade den nya CC-dosalgoritmen på ökade likheter gentemot MC-dosalgoritmen jämfört med den gamla CC-dosalgoritmen. Utjämningsfiltrets energifluensspektrum påverkade dosen i penumbraregionen måttlig. Resultatet från simuleringar i heterogena fantom visade att båda CC-dosalgoritmerna överskattade dosen i områden med lågdensitet jämfört med MC-dosalgoritmen. Överskattningen anses vara en konsekvens av ökad lateral spridning av elektorer i lågdensitetsområden som inte förutsägs av CC-dosalgoritmen.

Förslaget var att fortsätta utveckla den nya dosalgoritmen för att på ett korrekt sätt införa kärnvridning i en eventuell ny produktversion av CC-dosalgoritmen.

Acknowledgement

This thesis is an examining part in the completion of my master's degree in Engineering Physics at KTH Royal Institute of Technology. The thesis was carried out at RaySearch Laboratories AB. I am grateful to RaySearch Laboratories and my supervisor Björn Hårdemark who formulated the problem in this thesis and has supported me with inspiring ideas, motivation and feedback during this process.

In addition, I would also like to thank my colleagues at the Research Department for the support and thoughts during this master's thesis, especially Tore Ersmark.

Finally I would like to thank my supervisor Hans Bornefalk from KTH for feedback on the scientific content in this master's thesis.

Victor Löf, June 2015

Table 1: Abbreviations used in this thesis and sections where they are further explained.

CC	Collapsed Cone	1.3, 2.7.1 and 2.8.1
MC	Monte Carlo	1.4, 2.7.2 and 2.8.2
CT	Computed Tomography	1.2
MRI	Magnetic Resonance Imaging	1.3
PET	Positron Emission Imaging	1.3
TPS	Treatment Planning System	1.3
TERMA	Total Energy Released per unit Mass	2.7.1
KERMA	Kinetic Energy Released per unit Mass	2.4.1
VMC	Voxel Monte Carlo	2.7.2
EGSnrc	Electron Gamma Shower national research council	2.7.2
SSD	Source-to-Surface Distance	3
Linac	Linear Accelerator	1.1 and 2.5
ERT	External Radiation Therapy	1.1

Contents

Chapter 1

Introduction

1.1 Cancer Incidence and Treatment Methods

Cancer is a collective name for diseases with abnormal cell growth. The mortality of cancer is decreasing in Sweden even though the number of people diagnosed with cancer is increasing. Cancer is treated with different methods and combinations of methods depending on the type and the stage of the cancer. Radiation therapy is one commonly used treatment method. It uses high-energy radiation focused on the tumor region to kill the abnormal tumor cells and spare the surrounding healthy cells. The particles used in radiation therapy can be of different kinds e.g., ions, protons, electrons or photons. The radiation can be delivered with External Radiation Therapy (ERT) or internal radiation therapy. In ERT, the source of irradiation is located outside the patient body. The most common particle type in ERT is the photon. Photons are generated in linear accelerators (Linacs), which are mounted on a mechanical gantry and can be rotated around the patient to get focused radiation [3].

1.2 External Radiation Therapy with Photons

External radiation therapy with photons has advantages and disadvantages compared to ERT with other particles. One advantage of photons is that they are relatively cheap to produce compared to the other particles. Photons also have the advantage of being less dependent on uncertainties in the clinical process such as positioning of the patient and the Computed Tomography (CT) image data. One disadvantage of photons is their low relative biological effectiveness. Photons require a higher physical dose to achieve the same tumor damage compared to heavier particles such as ions [13].

1.3 Clinical Process in Radiation Therapy

The clinical treatment process in ERT with photons begins with the patient being imaged with a CT. The CT image can be complemented with images from imaging techniques such as Positron Emission Tomography (PET) or Magnetic Resonance Imaging (MRI) to decrease the uncertainty in the tumor localization. Given a localized tumor, the clinical process proceeds with a clinical team evaluating which volumes of the patient to irradiate. The images where the volumes are delineated are imported to a Treatment Planning System (TPS) [11]. The TPS is a tool used to create an optimal treatment plan for the patient, a process which requires simulations of dose distributions. One such TPS is called RayStation and is developed by RaySearch Laboratories. The clinically used dose calculation algorithm in RayStation is called the Collapsed Cone (CC) dose algorithm.

1.4 Problem Description

The goal of project is to study the differences between a CC based dose calculation algorithm and a prototype Monte Carlo (MC) based dose calculation algorithm available in a research version of RayStation v.4.8.0. Study the differences in water to see if there are identifiable patterns regarding, for instance, surface dose, out-of-field dose, small fields, large fields and large depths. If there are differences, investigate if they can be tied to some known approximation within the CC dose algorithm. Also, set up geometries for different types of inhomogeneities and perform a similar analysis. If this can be successfully executed within the project, also study model changes that would affect both the dose algorithms, such as separating the flattening filter source and calculating its dose with a separate energy fluence spectrum. If there is even more time, study if some aspect of the CC dose algorithm can be further improved such as removing the so called no kernel tilt approximation.

Chapter 2

Theoretical Background

In 1905, Albert Einstein published a paper on the photoelectric effect where the photon is treated like a particle [5]. A number of applications followed such as X-ray imaging and scientists became aware of photon interactions with matter and new fields such as radiation dosimetry and radiation therapy were introduced.

This chapter concerns the basic physical processes of photon interactions and their quantities, how photons are generated, photon dose distribution in homogeneous materials as well as the theory and the implementation of the different dose algorithms in the TPS.

2.1 Sources of Photon Radiation

Ionizing photon radiation can be classified in four categories depending on their origin:

1. Bremsstrahlung: Continuous energy spectrum of X-rays resulting from electron–nucleus Coulomb interactions.

2. Characteristic X-rays: Discrete energy spectrum of X-rays resulting from transitions of orbital electrons from one allowed atomic shell to a vacancy in another atomic shell.

3. Gamma radiation: Discrete X-rays emitted through nuclear transitions in gamma de-excitation.

4. Annihilation radiation: Discrete X-ray spectrum resulting from positron–electron annihilation.

Photons are also divided into different categories depending on their energy, see Table 2.1.

The photon energies used in radiation therapy applications are often in the mega voltage energy range [13].

Table 2.1: Categorization of photon energies.

Photon beam energy	**Terminology**
0.1–20 kV	Low energy X-rays
10–120 kV	Diagnostic range X-rays
120–300 kV	Orthovoltage X-rays
300 kV–1 MV	Intermediate energy X-rays
>1 MV energy	Mega voltage X-rays

2.2 Photon Interactions with Matter

Photons are indirectly ionizing radiation and deposit energy in a two-step process:

1. The photon interacts with the absorber and a charged particle is released e.g., an electron or a positron.

2. The charged particle deposits energy through Coulomb interactions with electrons in the absorber.

Incident photons upon an absorber cause a cascade of electromagnetic interactions. The following sections describe the most important photon interactions in radiation therapy and their quantities.

2.2.1 Cross Section and Attenuation Coefficient

Interaction processes can be defined in terms of cross section σ and attenuation coefficient μ. These two concepts are defined from photons incident on a target with the intensity I, the target thickness dx and the number of atoms per unit volume N. The fractional reduction in intensity is given by

$$\frac{dI}{I} = -\sigma N\, dx = -\sigma \frac{\rho N_{\mathrm{A}}}{A}\, dx = -\mu\, dx, \tag{2.1}$$

where ρ is the density of the absorber, N_{A} is Avogadro's number and A is the atomic mass of the absorber.

The linear attenuation coefficient is used to characterize the probability of an interaction. Given the linear attenuation coefficient μ and a target thickness x, the intensity $I(x)$ can be calculated as

$$\int_{I(0)}^{I(x)} \frac{dI}{I} = \int_0^x \mu\, dx' \rightarrow I(x) = I(0) e^{-\int_0^x \mu\, dx'}. \tag{2.2}$$

The total linear attenuation coefficient is the sum of individual linear attenuation coefficients from the photoelectric effect, Compton scattering, Rayleigh scattering, and pair production.

The relative predominance of individual cross sections is dependent on the energy of the incident radiation and the atomic number of the absorber. The photoelectric effect is the dominant effect for absorbers with high atomic numbers and photon energies from soft X-rays to orthovoltage X-rays. Compton scattering is the dominant effect for mega voltage X-rays energies and for even higher energies pair production is the dominant effect [13].

2.2.2 Photoelectric Effect

The photoelectric effect occurs when a photon interacts with an electron that is tightly bound to the nucleus. The interaction leads to a complete absorption of the photon and an ejection of a photoelectron. An electron from a higher energy state fills the vacancy created. The energy from the transition is released in the form of a characteristic X-ray or an Auger electron. The photoelectric cross section is inversely proportional to the photon energy to the power of three and directly proportional to the atomic number of the absorber to the power of four [13].

2.2.3 Compton Scattering

Compton scattering occurs when a photon interacts with a loosely bound electron. A part of the photon energy is transferred to the electron. As a result, the photon is scattered with a certain angle and a Compton electron is ejected from the atom. The Compton scattering cross section decreases with energy and is directly proportional to the atomic number of the absorber [13].

2.2.4 Pair Production

Pair production occurs when a photon interacts with the Coulomb field of the nucleus, gets absorbed and creates an electron–positron pair. The interaction has a threshold energy of 1.022 MeV, equal to the rest energy of two electrons. The pair production cross section increases with increasing energy and is directly proportional to the atomic number of the absorber to the power of two [13].

2.2.5 Photonuclear Effect

The photonuclear effect occurs at photon energies above 7–8 MeV. The photon interacts directly with the nucleus and gets absorbed. An emission of a neutron, proton or other charged particle occurs follows the photon absorption. The photonuclear effect is often neglected even though it may contribute as much as 5% of the total cross section at 20 MeV [13].

2.3 Electron Interactions with Matter

An electron interacts with both orbital electrons of the atoms and the nuclei of the atoms. A collision between an incident electron and an atom may be elastic and

inelastic. An elastic interaction leads to a deflection of the original path without any energy loss, while an inelastic interaction leads to an energy loss either via collisional losses or radiative losses. The collisional losses are due to ionization and excitation events. Radiative losses are due to Bremsstrahlung processes [13].

2.3.1 Stopping Power

The energy loss per unit path length of a charged particle is called stopping power. The stopping power can be divided in to collision stopping power and radiation stopping power. The former decreases and the latter increases for an increased atomic number Z of the absorber. The stopping power dT/dx is described by the Bethe-Bloch theory for electrons as

$$-\frac{dT}{dx} = \frac{2\pi e^4}{m_0 v^2} NB, \tag{2.3}$$

where

$$B = Z\left(\ln\frac{m_0 v^2 T}{2I^2(1-\beta)^2} - (\ln 2)(2\sqrt{1-\beta^2} - 1 + \beta^2) + 1 - \beta^2 + (1/8)(1-\sqrt{1-\beta^2})^2\right) \tag{2.4}$$

and v is the velocity of the electron, N is the number density of the absorber, Z is the atomic number of absorber, m_0 is the electron rest mass, e is the electron charge, I is an experimental parameter representing the average excitation and ionization potential, B is known as the stopping number and β is v/c where c is the speed of light [13].

2.4 Dosimetry

Radiation dosimetry quantifies the energy released to an absorber given the different interaction processes described in the previous section. This section describes how radiometric quantities and interaction quantities are combined into dosimetric quantities.

2.4.1 Radiometric Quantities

The radiant energy R is defined as the product of the particle number N and the particle energy E. The particle number is often dependent on particle type i, point of interest $\mathbf{r}$, E, time t and movement direction $\mathbf{\Omega}$. The energy fluence Ψ is defined as the product between the photon fluence Φ and the particle energy [13].

2.4.2 Energy Transferred and Kinetic Energy Released per Unit Mass

Energy transferred $\varepsilon_{\mathrm{tr}}$ is the kinetic energy transfer to charged particles in a specific finite volume V given by

$$\varepsilon_{\mathrm{tr}} = R_{\mathrm{in}}^{\mathrm{u}} - R_{\mathrm{out}}^{\mathrm{u,nonr}} + \sum Q, \tag{2.5}$$

where $R_{\mathrm{in}}^{\mathrm{u}}$ is the radiant energy of uncharged particles entering V, $R_{\mathrm{out}}^{\mathrm{u,nonr}}$ is the radiant energy of uncharged particles leaving V, except that which originated from radiative losses of kinetic energy by charged particles while in V and $\sum Q$ net energy derived from rest mass in V.

KERMA K is the energy transferred to charged particles per unit mass including radiative energy losses, but excluding energy passed from one charged particle to another. K is defined as [13]

$$K = \frac{d\varepsilon_{\mathrm{tr}}}{dm}. \tag{2.6}$$

Energy Imparted and Absorbed Dose

Energy imparted ε is defined as the sum of all energy deposits in a small volume V as

$$\varepsilon = R_{\mathrm{in}}^{\mathrm{u}} - R_{\mathrm{out}}^{\mathrm{u}} + R_{\mathrm{in}}^{\mathrm{c}} - R_{\mathrm{out}}^{\mathrm{c}} + \sum Q, \tag{2.7}$$

where R_{in}^{u} is radiant energy of uncharged particles entering V, R_{out}^{u} is radiant energy of uncharged particles leaving V, R_{in}^{c} is radiant energy of charged particles entering V, R_{out}^{c} is radiant energy of charged particles leaving V and $\sum Q$ is net energy derived from rest mass in V.

The absorbed dose D is the energy imparted to matter per unit mass at a point as [13]

$$D = \frac{d\varepsilon}{dm}. \tag{2.8}$$

2.5 Linear Accelerators

Photons in ERT are generated in Linacs. The following section describes the photon generation and the beam shaping in the treatment head. The different components in a treatment head can be seen in Figure 2.1.

2.5.1 Electron Acceleration

The photons are produced by focusing accelerated electrons on a metal target. The electrons are generated by an electron gun. The electron gun consists of a filament that upon heating and within an electrostatic field releases electrons. The strength

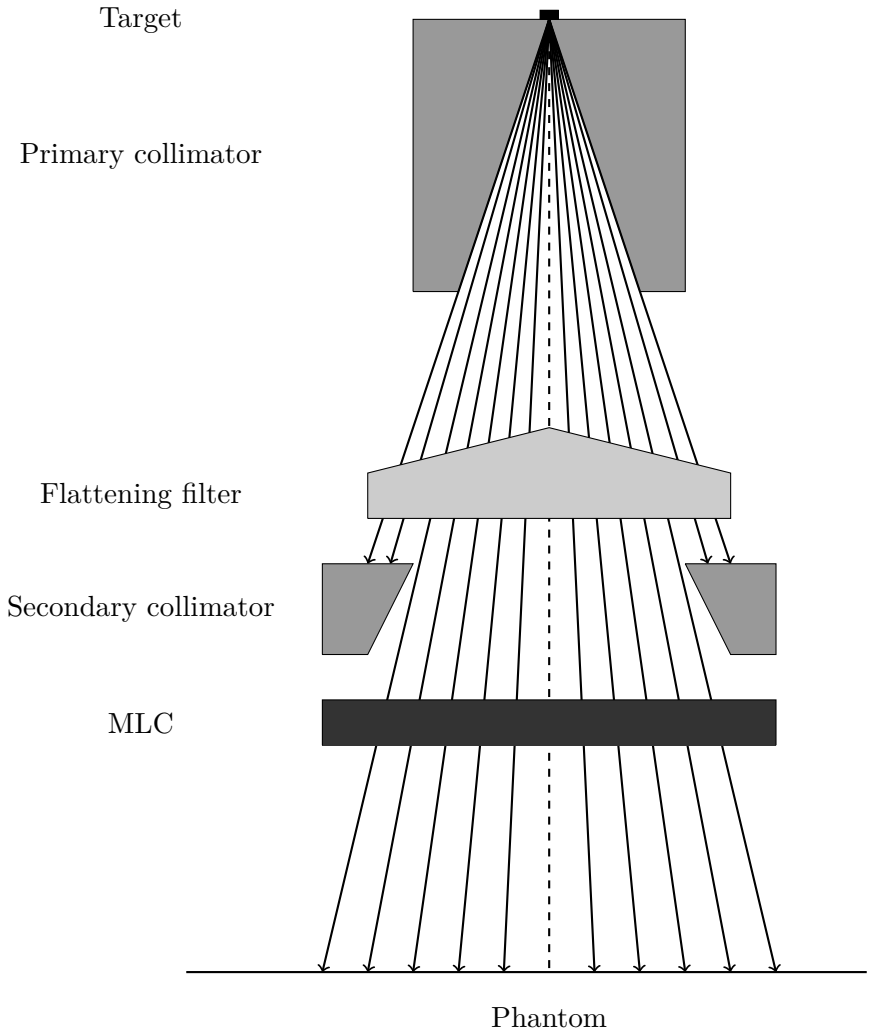

Figure 2.1: Illustration of the treatment head for photons.

of the current in the filament regulates the electron fluence in the Linac and thereby the fluence of photons [11].

2.5.2 Photon Production

The accelerated electrons strike the metal target and produce photons. The aims of the photon production are high bremsstrahlung production, high mean energy, small source size, a large angular distribution and a low electron contamination. The following sections describe the components of a treatment head [11].

Target Design

The target consists of metal with high atomic number Z to get a high production rate of bremsstrahlung since it is proportional to the atomic number of the target to the power of two.

However, a too high atomic number decreases the amount of bremsstrahlung in the forward direction and a too thick target leads to low photon fluence due to self-attenuation. The aims are often achieved with a Tungsten target with a thickness of one third of the electron range. The photons produced in the target are then collimated in the primary collimator, see Figure 2.1 [11].

Flattening Filters

After the primary collimator there is a flattening filter. The function of the flattening filter is to make the beam intensity distribution uniform across the field. This is achieved by designing flattening filters that have a material with a high atomic number in the center and a material with a low atomic number in the periphery. The use of flattening filters leads to more electron contamination and a decreased photon beam fluence. For that reason, the use of flattening filters has declined in modern ERT. After the flattening filter the beam is further collimated before it reaches the patient [11].

2.6 Photon Dose Distribution in Homogeneous Materials

The photon energy fluence is affected by the inverse-square law as well as attenuation and scattering of the photon beam inside the patient. The representation of dose distribution can be divided into different categories. Depth dose curves are dose distributions along a line parallel to the beam propagation direction. Lateral dose curves are dose distributions a long a line perpendicular to the beam propagation direction at a certain depth [11].

2.6.1 Depth Dose Curves

Areas of interest in a depth dose curve include the surface dose, the maximum dose and the exit dose. The surface dose is dependent on the photon beam energy and on the field size. One of the contributors to the surface dose is scattered photons from collimators, flattening filters and air in the beam line. A second contributor to the surface dose is backscattered photons from the patient. A third contributor is high-energy electrons produced by interactions in the beam line. The surface dose is decreased for higher photon energies.

Following the surface dose there is a build-up region. This is due to the relatively long ranged secondary electrons created at the patient surface.

The maximum dose is reached at the end of the build-up region. The depth at which the maximum dose occurs depends on the energy and the field size of the beam. The maximum dose occurs at deeper depths for increased photon energies.

Depending on the density of the material behind the patient the exit dose may have a build-up region or build-down region due to a decreased or increased amount of backscattered electrons [11].

2.6.2 Lateral Dose Curves

Areas of interest in a lateral dose curve include the central region, the penumbra region and the umbral region. The central region is the portion of the beam from the central axis within 1 cm to 1.5 cm of the geometric field edges.

The penumbra region is defined as the integral from 20% of the maximum dose to 80% of the maximum dose. This integral should ideally be close to zero to optimize the beam shape at the field edges. Three main processes create the penumbra region. A geometrical spread of intensity at the field edges is seen since the source if of finite size. Scatter in the patient blurs the edges of the field. Finally, there is a possibility of transmission through the collimators which also contributes to the penumbra.

The umbral region defines the dose outside the target volume. This area should be close to zero to minimize the dose delivered to organs and tissue outside the target volume [11].

2.7 Theory of Dose Algorithms

There are several ways to calculate dose distributions. The CC based dose calculation algorithm uses kernel based convolution and superposition. The kernels represent the transport of energy or dose from an interaction point and are precalculated with MC simulations. The MC based dose calculation uses statistical methods to calculate dose. The following sections describe the basic theory of CC and MC [2].

2.7.1 Collapsed Cone

A collapsed cone based dose calculation algorithm is based on a separation of primary photon transport and secondary transport of photons and electrons. The Total Energy Released per unit Mass (TERMA) represents the primary photon transport. TERMA is defined for a point $\mathbf{r}$, photons of energy E and an energy fluence $\Psi_E(\mathbf{r})$ in a medium of a density $\rho(\mathbf{r})$ as

$$T_{\mathrm{E}}(\mathbf{r}) = (r/r_0)^2 \frac{\mu(E,\mathbf{r})}{\rho(\mathbf{r})} \Psi_E(\mathbf{r_0}) \exp\left(\int_{\mathbf{r}_0}^{\mathbf{r}} -\mu(E,l)\, dl\right), \tag{2.9}$$

where $\mu(E,\mathbf{r})$ is the linear attenuation coefficient of the absorber at $\mathbf{r}$ and $\Psi_E(\mathbf{r_0})$ is the energy fluence differential in energy on a reference plane [1].

Point-spread kernels $h(E, \mathbf{s}, \mathbf{r})$ represent the secondary transport of electrons and photons. These give the distribution of energy or dose to a point $\mathbf{r}$ from a single photon interaction at a point $\mathbf{s}$ in water. The point-spread kernels are often pre-calculated with MC simulations for discrete energies. Mono-energetic point-spread kernels can be combined into poly-energetic point-spread kernels by appropriate weighing according to the energy spectrum at a certain radiological depth, taking depth hardening and off-axis softening effects into account [1].

For poly-energetic kernels in homogeneous media the point-spread kernel function becomes spatially invariant and the analytical expression for dose to a point $D(\mathbf{r})$ is defined as

$$D(\mathbf{r}) = (1/\rho(\mathbf{r})) \int \iiint T_E(\mathbf{s})\rho(\mathbf{s})h(E, \mathbf{s}, \mathbf{r})\, d^3s\, dE, \tag{2.10}$$

where s is the point of the primary interaction, h is the point-spread kernel, T_E is the TERMA as in Equation 2.9 and ρ is the mass density. Equation 2.10 requires a lot of computational time. The CC dose algorithm decreases the computational time by collapsing the kernels into a certain number of directions. All the energy or dose is allocated to rectilinear directions emerging from the interaction point. This efficiently simplifies and reduces the number of scatter directions from the kernel [1].

2.7.2 Monte Carlo

MC simulations are widely used in medical physics. MC simulation is based on a statistical model that calculates the dose distribution given a limited set of particle interaction types and their probabilities. The probability for a certain interaction is given by the linear attenuation coefficient. The statistical fluctuation of the simulation process is decrease as the number of simulated photons per voxel is increased. MC dose calculations requires a lot of computational time and several different MC algorithms have been developed to decrease the calculation time e.g., Voxel Monte Carlo (VMC++) and Electron Gamma shower NRC (EGSnrc). However, the main idea behind MC algorithms can be summarized into four steps:

1. Estimate the distance to the next interaction. This is done with the probability for an interaction given by the linear attenuation coefficient.

2. Transport the particle to the interaction point.

3. Estimate the interaction type with the probability for individual interactions given by the attenuation coefficient for different interactions.

4. Simulate the interaction type.

This process is repeated until the original particle and all secondary particles have left the defined geometry or have been absorbed [4].

2.8 Implementation of Dose Calculation Algorithms

This section describes the implementation of the dose calculation algorithms.

2.8.1 The Collapsed Cone Dose Algorithm

The CC dose algorithm calculates dose in three steps. The first step is the energy fluence computation, the second step is the TERMA computation and the last step is the point-spread kernel convolution. The following section describes the geometry input that the CC algorithm is based on and the three calculation steps.

Geometry Input

The phantom is imaged with a CT and the images provide information about the mass density ρ_m of the phantom, expressed in Hounsfield Units HU according to

$$HU = 1000 \left(\frac{\mu - \mu_{\mathrm{H_2O}}}{\mu_{\mathrm{H_2O}}} \right), \tag{2.11}$$

where μ is the linear attenuation coefficient and $\mu_{\mathrm{H_2O}}$ is the linear attenuation coefficient for water. The HU can be translated into mass density via a CT calibration table.

The photon attenuation needs to be recalculated to compute the radiological depth and the attenuation of a voxel at radiation therapy energies. For energies between 0.1 MeV and 10 MeV, Compton scattering dominates the attenuation. Compton scattering scales with the electron density of the material. Mass density ρ_{m} relates to electron density ρ_{e} at low energies as

$$\frac{\rho_{\mathrm{e-material}}}{\rho_{\mathrm{e-water}}} = \frac{\rho_{\mathrm{m-material}}}{\rho_{\mathrm{m-water}}} \frac{< Z/A >_{\mathrm{material}}}{< Z/A >_{\mathrm{water}}}, \tag{2.12}$$

where $< Z/A >$ is the weighted mean nuclear ratio. The importance of pair production increases at higher radiation therapy energies. This effect is accounted for by calculating the effective density $\rho_{effective}$ as

$$\rho_{\mathrm{effective-material}} = \frac{\rho_{\mathrm{e-material}}}{\rho_{\mathrm{e-water}}} \frac{1 + \alpha(1 + < Z >_{\mathrm{material}}) \ln(E) E}{1 + \alpha(1 + < Z >_{\mathrm{water}}) \ln(E) E}, \tag{2.13}$$

where E is the photon energy in MeV and $< Z >$ is

$$< Z >= \frac{\sum_i f_i (Z^2/A)}{< Z/A >}, \tag{2.14}$$

where f_i is the weight fraction of atom type i in the material and α is $1.775 \cdot 10^3$ [14]. The effective density is calculated for the entire dose grid and radiological depths can be calculated from the effective density $\rho_{\mathrm{effective}}$ as

$$d(\mathbf{r}) = \int_{\mathbf{r_0}}^{\mathbf{r}} \rho_{\text{effective}}(\mathbf{r}, E_i)\, dl, \tag{2.15}$$

where $\mathbf{r_0}$ is the point where the ray crosses a arbitrary reference surface, E_i is the discrete energy and $\mathbf{r}$ is the position.

Energy Fluence Computation

The energy fluence computation consists of two sources called the primary source and the secondary source. The primary source models the target and the secondary source models the flattening filter, see Figure 2.1.

The two sources are projected through the collimators onto the fluence plane. The resolution of fluence grid is 1 mm × 1 mm for the primary source and 3 mm × 3 mm for the secondary source.

The sources are modeled with Gaussian intensity profiles. The primary source has an elliptical intensity profile and characterized by the dimensions of the target. The secondary source has a circular Gaussian intensity profile. Given the radiological depth $d(\mathbf{r})$ given by Equation 2.15, the primary energy fluence can be defined as

$$\Psi(d(\mathbf{r}), E_i) = \Psi_0 e^{-\mu(E_i) d(\mathbf{r})}, \tag{2.16}$$

where Ψ_0 is the energy fluence in the reference plane. Beam divergence is taken into account by applying the inverse-square law of Equation 2.16.

Total Energy Released per unit Mass Computation

TERMA T is calculated at a point $\mathbf{r}$ as

$$T(\mathbf{r}) = \int \frac{\mu(\mathbf{r}, E_i)}{\rho_{\text{m}}(\mathbf{r})} \Psi(d(\mathbf{r}), E_i)\, dE, \tag{2.17}$$

where $d(\mathbf{r})$ is the radiological depth, E_i is the discrete energy, ρ_m is the mass density, μ is the linear attenuation coefficient and Ψ is the energy fluence.

Point-Spread Kernels

The point-spread kernels used in the CC dose algorithm are pre-calculated with EGSnrc MC system originally developed for high-energy physics simulations at Stanford Linear Accelerator Center [9]. The kernels were generated in a homogeneous sphere with radius 90 cm in the material "H205212ICRU". The primary photon was forced to interact in the center of the sphere and transports 59.6 cm from the interaction were used for scoring. The electron transport cut-off energy was set to 512 keV and the photon cut-off energy was set to 10 keV. The point-spread kernels are transformed from a high-resolution 2D polar regular grid to a

lower resolution 2D grid with irregular intervals in θ. The intervals in θ are chosen to minimize the polar redistribution of energy. In the φ the angular bins are spatially evenly distributed. The total number of trace directions is the product between the number of θ-intervals and the number of ϕ-intervals. The standard is 8 θ intervals and 16 φ-intervals leading to 128 trace directions.

Superposition and Convolution

Each voxel with significant TERMA creates a point-spread kernel. The point-spread kernel is calculated from the energy spectrum corresponding to the radiological depth, off-axis softening and beam hardening of the calculation point. The dose is calculated from a dose point-of-view. Meaning the the dose is collected by tracing out in different angular directions. Moving out in a trace direction, the contribution from an intersected voxel is calculated by integrating the kernel over the radiological intersection length and scaling it with the TERMA for the intersected voxel, see Figure 2.2. This process is iterated for all the intersected TERMA voxels in all trace directions.

Algorithm Approximations and Weaknesses

The CC dose algorithm uses a number of approximations to increase the calculation speed. The calculation time t scales as

$$t \propto (N_{\mathrm{x}} N_{\mathrm{y}} N_{\mathrm{z}})^{4/3} N_{\theta} N_{\varphi}, \tag{2.18}$$

where N_{x} is the number of voxels in the x-direction and similarly for N_{y} and N_{z}. N_{θ} and N_{φ} are the number of directions in θ and φ.

In the CC dose algorithm, all the point-spread kernels are aligned with the central beam axis. Meaning that no tilting of the kernels off-axis. This is called the no kernel tilt approximation. The no kernel tilt approximation is compensated for by applying an inverse-square law de-scaling of the TERMA and then a corresponding re-scaling of dose as proposed by N. Papanikolaou [12]. This approximation increases the speed of the algorithm since it allows for a re-use of ray traces when sampling the TERMA distribution.

Unnecessary calculation time is further avoided by applying a calculation mask around the TERMA region. The tracing stops when there is no TERMA above 0.5% of the maximum TERMA within 5 cm radiological distance in a trace direction. These two parameters are called the TERMA cut-off fraction and radiological trace distance cut-off respectively.

2.8.2 Monte Carlo Dose Algorithm

The MC dose calculation algorithm uses the same energy fluence computation as the CC dose algorithm. The in-patient dose calculation is based on a VMC++ algorithm optimized for dose calculation in three dimensional voxel geometries. The

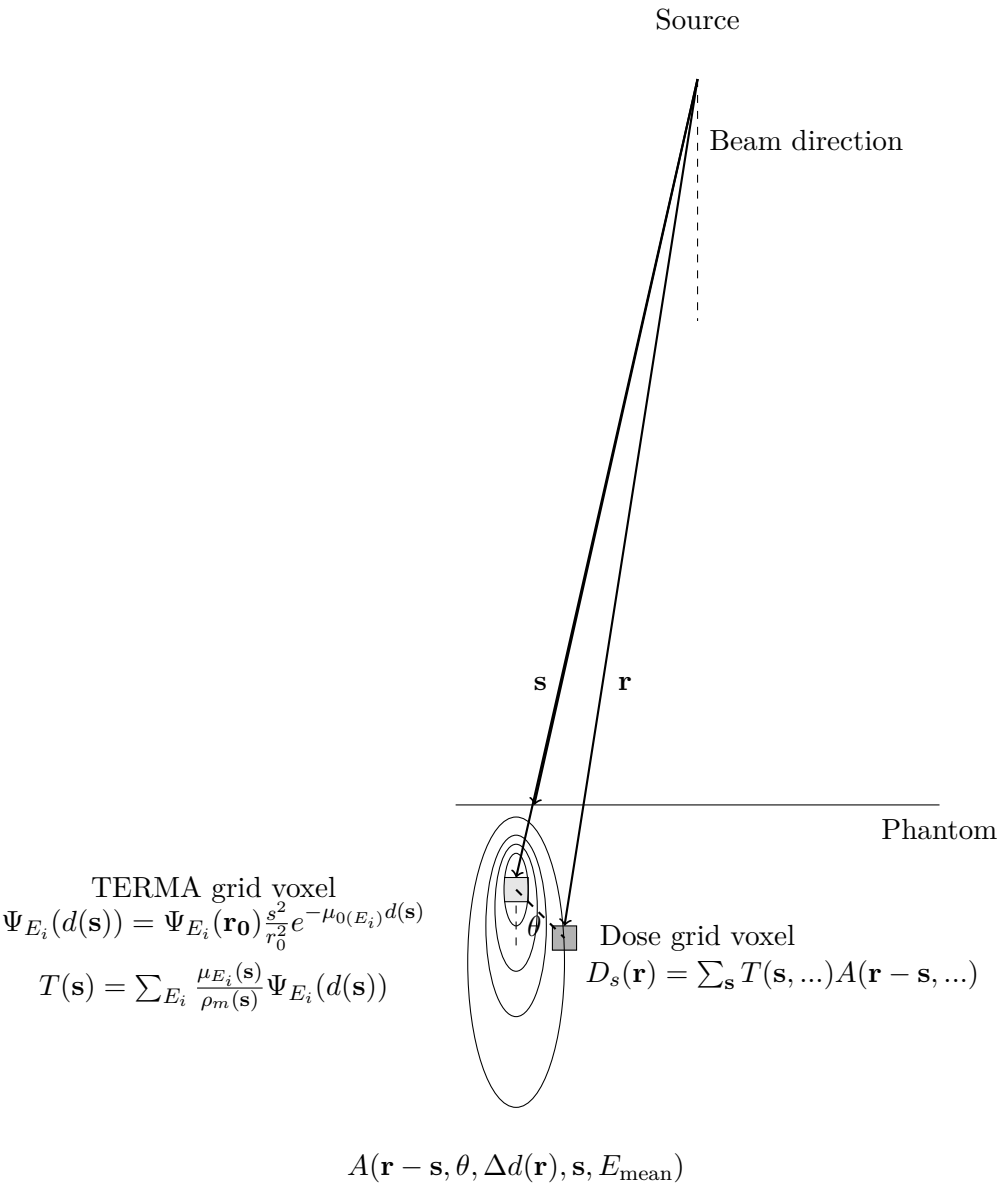

Figure 2.2: Illustration of the CC dose calculation algorithm.

algorithm uses a Class II condensed history scheme for charged particle transport. Condensed schemes are based on the observation that a vast majority of electron interactions lead to very small changes in the electron energy and direction. It is therefore possible to group many of these interactions into relatively few condensed steps. In the class II condensed scheme, interactions are categorized into hard and soft collisions. Soft collisions are condensed while hard collisions are explicitly simulated. The VMC++ algorithm scores dose-to-water [8].

2.8.3 Dose-to-Water

Dose can be reported as dose-to-water or dose-to-medium. The tradition within radiation therapy is to report dose as dose-to-water and thereby treat all materials as water with different densities [10].

Dose-to-water can be explained as the dose deposited to a specific point if an infinitesimal volume of tissue is replace with an infinitesimal volume of water. The CC dose algorithm calculates dose as dose-to-medium and later converts it to dose-to-water. There are two reasons for reporting dose-to-water:

1. It has been a tradition and a benchmark.

2. It is said to be clinically relevant since the radiation sensitive parts of the cell are surrounded by water [15].

The dose in Raystation computes the dose as dose-to-medium and then converts it do dose-to-water.

Chapter 3

Method

Simulations were conducted with the CC dose algorithm and the MC dose algorithm in different simulation models. This chapter describes the simulations and the models used in the study, an overview can be seen in Table 3.1. The chapter was divided into simulations done in a water phantom and in three heterogeneous phantoms. All simulations were performed with a Source-to-Surface Distance (SSD) of 100 cm, except in the SSD variation model. The resolution of the dose grid was set to 0.25 cm cubic voxels creating a voxel space of 242 $\times$ 246 $\times$ 242 voxels. Interpolation between each voxel point lead to an interpolated voxel space of 483 $\times$ 491 $\times$ 483 voxels. The CC simulations were conducted with 32 angular θ bins and 32 angular φ bins, a TERMA cut-off fraction of 0.0% and a radiological trace distance cut-off of 100 cm as a standard.

Table 3.1: Overview of the parts in the study.

Phantom	**Study**
3.1 Water Phantom	3.1.1 Difference study
	3.1.2 No kernel tilt approximation
	SSD variation model
	Nine sub-field model
	Multi-fields model
	3.1.3 Flattening filter energy fluence spectrum
	Flattening filter separation model
	3.1.4 New CC dose algorithm
3.2 Heterogeneous Phantoms	3.2.1 Difference study
	Heterogeneous phantom one
	Heterogeneous phantom two
	Heterogeneous phantom three

Two machine models were used in the simulations. The first machine model was a realistic 6 MV Linac referred to as the realistic machine. The second machine model was a Linac with a monochromatic 2 MeV energy spectrum without a flat-

tening filter, infinitesimal source size and no electron contamination referred to as the simplified machine.

3.1 Water Phantom

The water phantom had the dimensions of 60 cm × 60 cm × 60 cm and the density of 1.00 g/cm^3.

3.1.1 Difference Study

Simulations were conducted with the realistic machine and the simplified machine to study differences between the CC dose algorithm and the MC dose algorithm.

3.1.2 No Kernel Tilt Approximation

Several simulation models studied the effect of the no kernel tilt approximation with the simplified machine. The first simulation model studied the approximation by varying the SSD from 100 cm to 600 cm. An increased SSD would decrease the beam divergence and therefore the dependence on the no kernel tilt approximation.

The second simulation model studied the approximation by analyzing how the two dose calculation algorithms gives in-scattered dose contribution to the central beam axis. This was done by dividing a 30 cm × 30 cm field into nine sub-fields as in Figure 3.1.

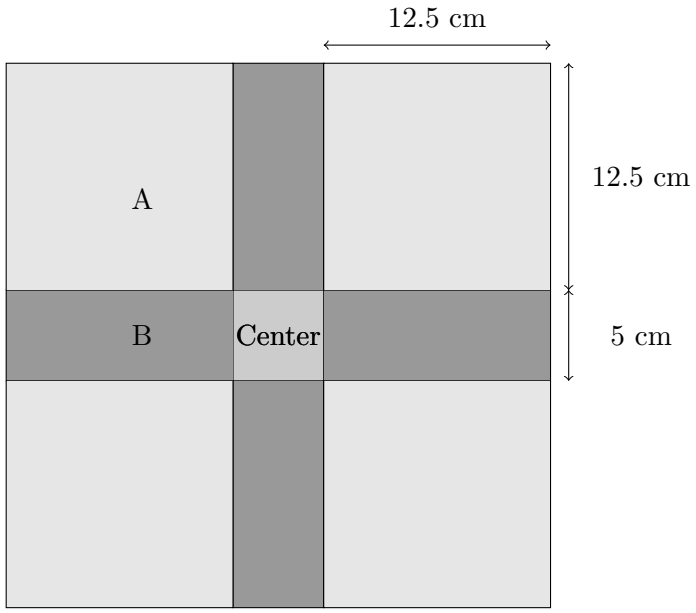

Figure 3.1: Illustration of the nine sub-field model.

The model estimated how much the difference in dose between the two dose calculation algorithms that was due to in-scatter from the field periphery. This was done for the depth dose on the central beam axis as

$$\frac{4\left(\left|D_{\mathrm{A}}^{\mathrm{CC}}(x)-D_{\mathrm{A}}^{\mathrm{MC}}(x)\right|+\left|D_{\mathrm{B}}^{\mathrm{CC}}(x)-D_{\mathrm{B}}^{\mathrm{MC}}(x)\right|\right)}{|D^{\mathrm{CC}}(x)-D^{\mathrm{MC}}(x)|}, \tag{3.1}$$

where x was the depth, $D_{\mathrm{A}}^{\mathrm{CC}}$ and $D_{\mathrm{A}}^{\mathrm{MC}}$ were the depth dose contribution from field A calculated with CC and MC respectively, $D_{\mathrm{B}}^{\mathrm{CC}}$ and D_{B}^{MC} were the depth dose contribution from field B calculated with CC and MC respectively, D^{CC} and D^{MC} were the depth dose for an entire 30 cm $\times$ 30 cm field calculated with CC and MC, respectively.

A third simulation model forced a discrete implementation of kernel tilt. The kernels were aligned with the central beam axis. The discrete kernel tilt implementation was forced by dividing the main field into 2 cm $\times$ 2 cm fields and tilting the central beam axis for each field, see Figure 3.2. All the axes converged at a point corresponding to a SSD of 100 cm. As a results, the central beam axis and the kernels tilted more for fields in the periphery than for fields in the center.

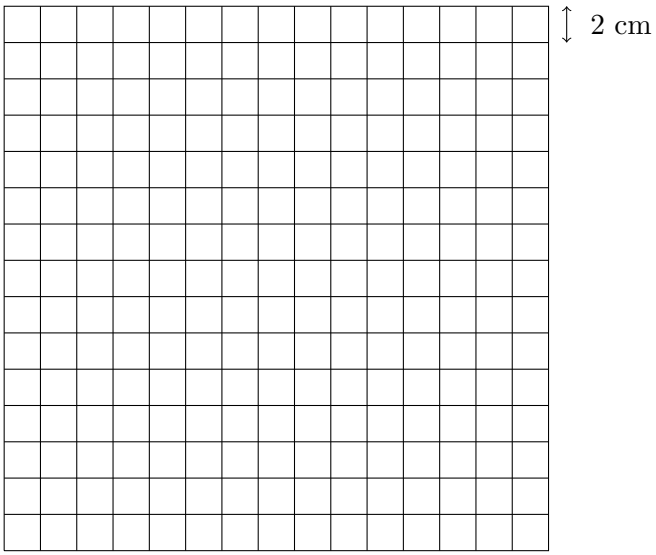

Figure 3.2: Illustration of multi-field model.

3.1.3 Flattening Filter Energy Fluence Spectrum

A flattening filter separation model studied the effect that the flattening filter energy fluence spectrum had on the dose distribution for a field size of 20 cm $\times$ 20 cm. This was done by separating the dose from the primary source and the flattening filter source. The separation made it possible to simulate the two source with different

energy fluence spectrums. In this model, the energy fluence spectrum of the primary source was held constant. The energy fluence spectrum of the flattening filter source was varied. Two different energy fluence spectrums were used and their mean energy can be seen in Figure 3.3. The total dose was given by combining the dose from the primary source and the flattening filter source. The combination had the weighed sum of one and the flattening filter weight was 0.06.

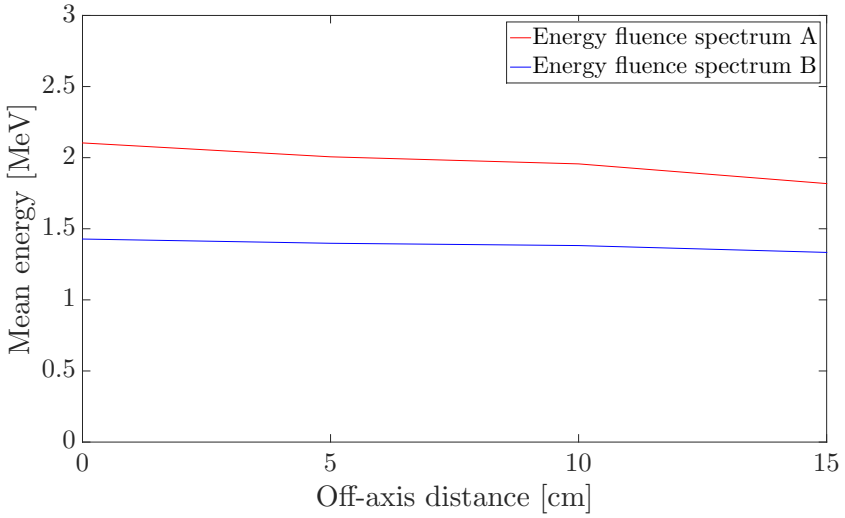

Figure 3.3: The mean energy of the two different energy fluence spectrums as a function of off-axis distance. Energy fluence spectrum A had a higher mean energy than the energy fluence spectrum B.

3.1.4 New CC Dose Algorithm

A new CC dose algorithm including an implementation of kernel tilt was simulated and evaluated against the old CC dose algorithm and the MC dose algorithm. Kernel tilt was implemented by tilting the polar sampling directions of the kernel and the trace directions. In addition, the kernels were radially cumulative dose kernels.

A scoring function was included in the evaluation. It calculated the mean relative error from 1 cm × 1 cm × 1 cm sample volumes placed in the dose distributions. The sample volumes were placed at the depths of 5 cm, 10 cm, 15 cm, 20 cm, 25 cm and 30 cm on the central beam axis, 2 cm inside the field edge and 2 cm outside the field edge. The mean relative error was calculated as

$$\sum_{i,j,k,l} \left| \frac{\left(\frac{CC_{i,j,k,l}}{CC_{\text{norm}}} - \frac{MC_{i,j,k,l}}{MC_{\text{norm}}} \right)}{N} \right|_l \Big/ N_{tot}, \tag{3.2}$$

where $CC_{i,j,k,l}$ and $MC_{i,j,k,l}$ were the dose at a point i, j and k in sample volume l calculated with CC and MC, respectively. CC_{norm} and MC_{norm} were the calibration points for CC and MC respectively, see Section 3.1.5. N was the number of voxels in the sample volume and N_{tot} was the total number of sample volumes.

3.1.5 Normalization

The dose calculated in the water phantom were normalized to a calibration point. The calibration point was the mean of points in a 1 cm × 1 cm × 1 cm volume centered around a point at a depth of 10 cm on the central beam axis.

3.2 Heterogeneous Phantoms

Simulations were done in three different heterogeneous phantoms with the simplified machine to compare the two dose algorithms in heterogeneous situations.

The first heterogeneous phantom can be seen in Figure 3.4. The simulations were preformed with the fat density 0.95 g/cm^3, the lung density 0.5 g/cm^3, the bone density 1.85 g/cm^3 and the air density 0.00121 g/cm^3. The phantom was irradiated with the field sizes of 2 cm × 2 cm, 3 cm × 3 cm and 5 cm × 5 cm. The dose was normalized to the dose at a depth of 7.5 cm as in Subsection 3.1.5.

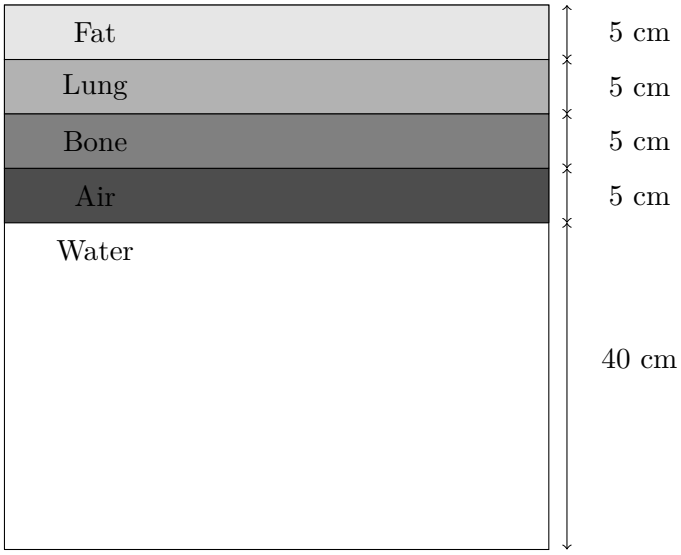

Figure 3.4: The first heterogeneous phantom. All the slabs had the width and length of 60 cm × 60 cm.

The second heterogeneous phantom can be seen in Figure 3.5. The simulations were preformed with the lung densities of 0.1 g/cm^3 and 0.24 g/cm^3. The phantom was irradiated with the field size of 5 cm × 5 cm. The dose was normalized to the dose at the depth of 9 cm as in Subsection 3.1.5.

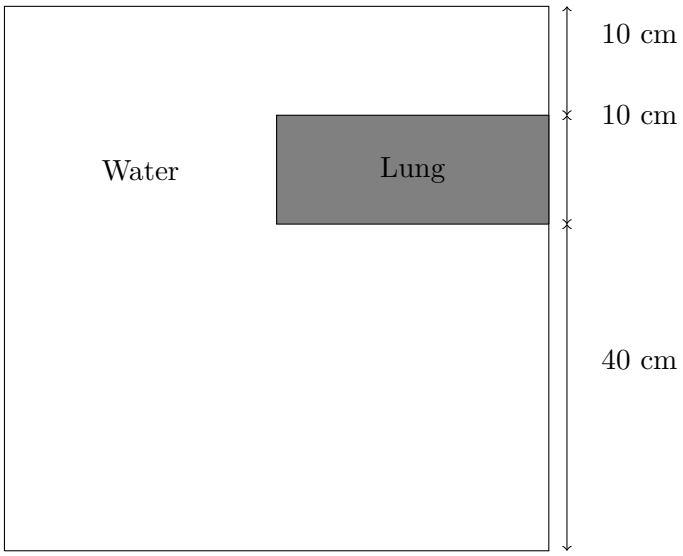

Figure 3.5: The second heterogeneous phantom. The lung slab had the width and length of 30 cm × 60 cm.

The third heterogeneous phantom can be seen in Figure 3.6. The simulations were performed with the air density 0.00121 g/cm^3, the water density 1.0 g/cm^3, the PMMA density of 1.19 g/cm^3 and the PMI foam density 0.066 g/cm^3. The phantom was irradiated with the field sizes of 5 cm × 5 cm and 10 cm × 10 cm.

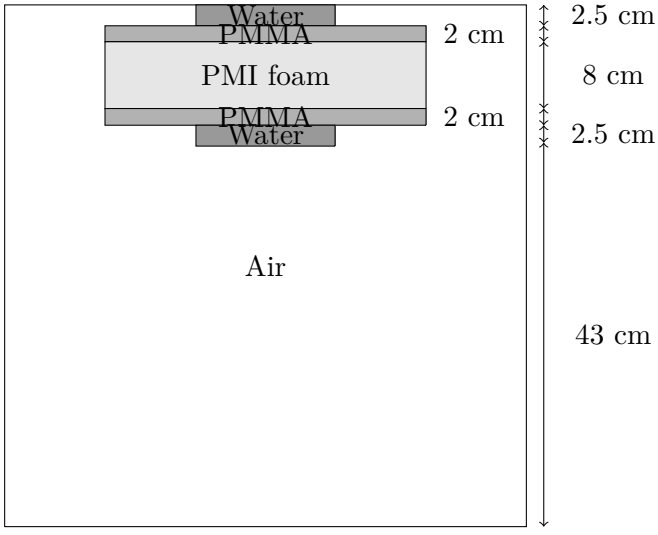

Figure 3.6: The third heterogeneous phantom. The water slabs had the width and length of 13 cm × 13 cm. The other slabs had the width and the length of 30 cm × 30 cm.

Chapter 4

Results and Discussion

This chapter contains chosen results from the simulations that were of interest to further analyze and discuss. The chapter was divided into results from the simulations done in the water phantom and in the three heterogeneous phantoms.

4.1 Results from the Water Phantom

4.1.1 Difference Study

The results from the simulations with the realistic machine in water showed significant differences in dose calculated with the two dose algorithms, see Figures 4.1 and 4.2. The CC dose algorithm overestimated the dose at shallow depths and underestimated the dose at deeper depths compared to the MC dose algorithm, see Figure 4.1. The same tendencies were seen in the penumbra region, see Figure 4.2.

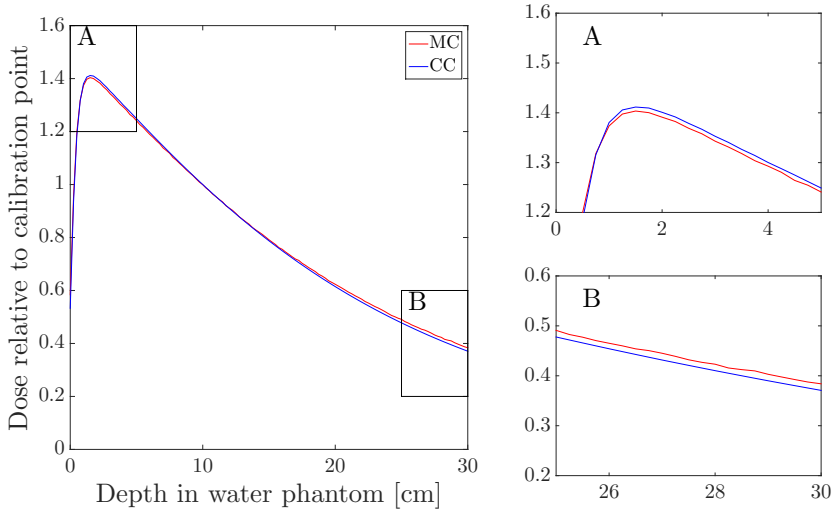

Figure 4.1: Simulations with the realistic machine in the water phantom. Showing the depth dose on the central beam axis calculated with the two dose algorithms. The field size was 20 cm × 20 cm. Subfigure A shows the maximum dose region and subfigure B shows the exit dose region.

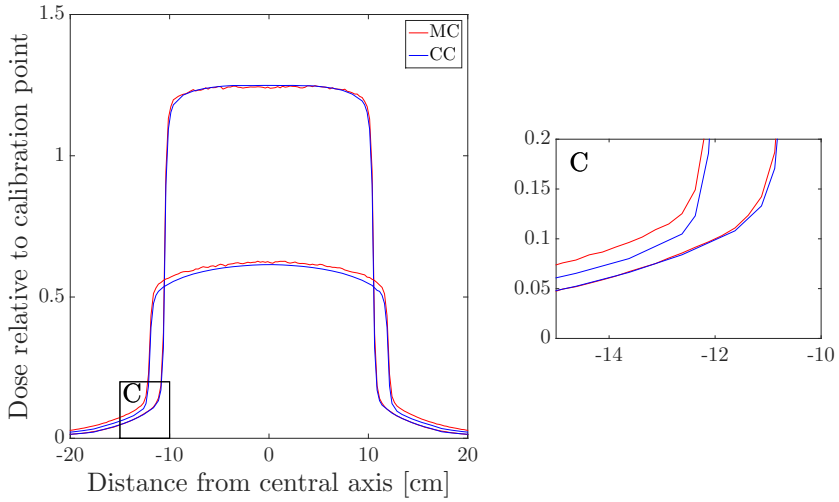

Figure 4.2: Simulations with the realistic machine in the water phantom. Showing the lateral dose at the depths of 5 cm and 20 cm calculated with the two dose algorithms. The field size was 20 cm × 20 cm. Subfigure A shows the penumbra region.

4.1.2 No Kernel tilt Approximation

To study the effect of the no kernel tilt approximation the machine model was simplified. The simplification to a monochromatic 2 MeV energy spectrum was done since it approximately corresponded to the mean energy of a realistic 6 MV Linac. Further simplifications were no electron contamination, no flattening filter and infinitesimal primary source size. These were potential contributors to the dose in the penumbra region and were turned off to further isolate the effect of the no kernel tilt approximation. The results from the simulations with the simplified machine in water showed similar tendencies as results from the simulations with the realistic machine, see Figures 4.3 and 4.4.

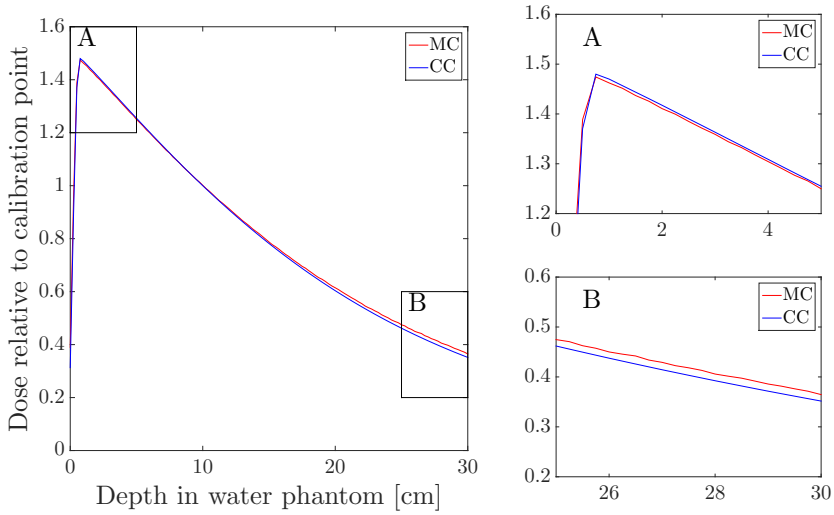

Figure 4.3: Simulations with the simplified machine in the water phantom. Showing the depth dose on the central beam axis calculated with the two dose algorithms. The field size was 20 cm × 20 cm. Subfigure A shows the maximum dose region and subfigure B shows the exit dose region.

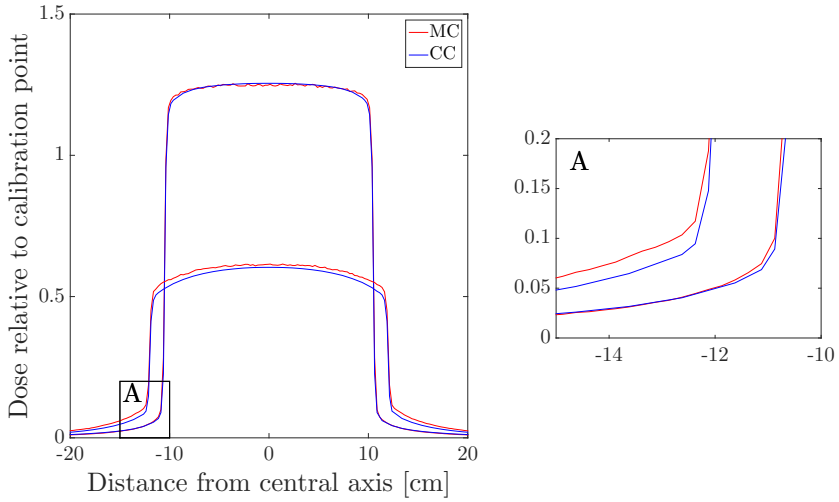

Figure 4.4: Simulations with the simplified machine in the water phantom. Showing the lateral dose at the depths of 5 cm and 20 cm calculated with the two dose algorithms. The field size was 20 cm × 20 cm. Subfigure A shows the penumbra region.

The first simulation model studied the no kernel tilt approximation by varying the SSD in the simulations. The hypothesis was decreased differences in dose calculated with the two dose algorithms for longer SSDs since the beam becomes less diverged and therefore less dependent on the no kernel tilt approximation. The hypothesis was confirmed by the results, see Figure 4.5. The dashed lines corresponding to the simulations done with a 600 cm SSD showed decreased differences compared to the solid lines corresponding to the simulations done with a 100 cm SSD.

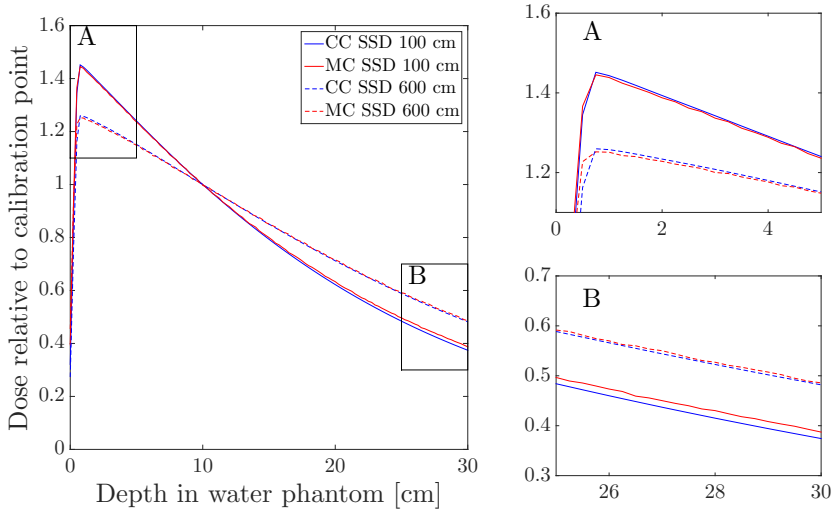

Figure 4.5: Simulations with the simplified machine in the water phantom. Showing the depth dose on the central beam axis for two different SSDs calculated with the two dose algorithms. The field size was 30 cm × 30 cm. Subfigure A shows the maximum dose region and subfigure B shows the exit dose region.

Further support for the no kernel tilt approximation as the primary cause of the differences between CC dose algorithm and MC dose algorithm was seen in the nine sub-field model. The model studied the effect that the field periphery had on the depth dose at the central beam axis, see Figure 4.6. The results showed that there were small differences between the two dose algorithms regarding the dose in the center field. However, there were significant differences in how the two dose algorithms calculated the in-scatter dose contribution from the periphery of the field. The model estimated that the differences in dose between the two dose algorithms on the central beam axis for a full 30 cm × 30 cm field were due to 80.0% and 71.5% from differences in-scatter contributions from the field periphery. The two estimations were done at the depths of 5 cm and 30 cm, respectively.

The results from the multi-field model can be seen in Figure 4.7. The multi-field model had an improved resemblance to the MC dose distribution outside the field compared to the CC dose algorithm. The noise in inside the field was due to slight overlapping field edges in the multi-field simulation model.

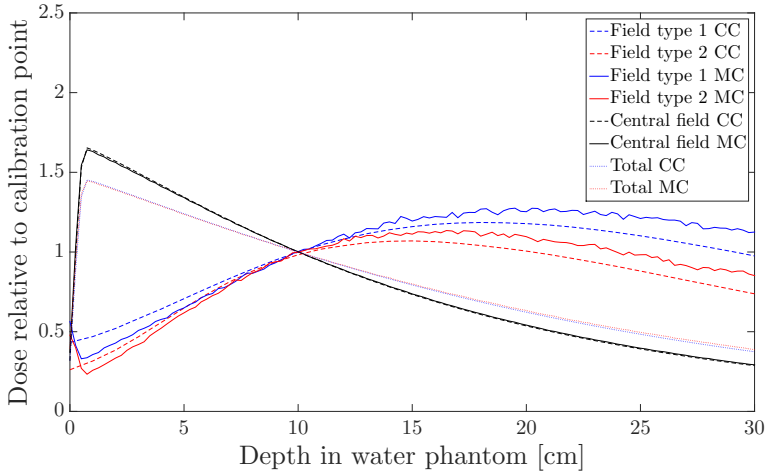

Figure 4.6: Simulations with the simplified machine in the water phantom. Showing the depth dose on the central beam axis for each sub-field in the nine sub-field model as well as for a full 30 cm × 30 cm field.

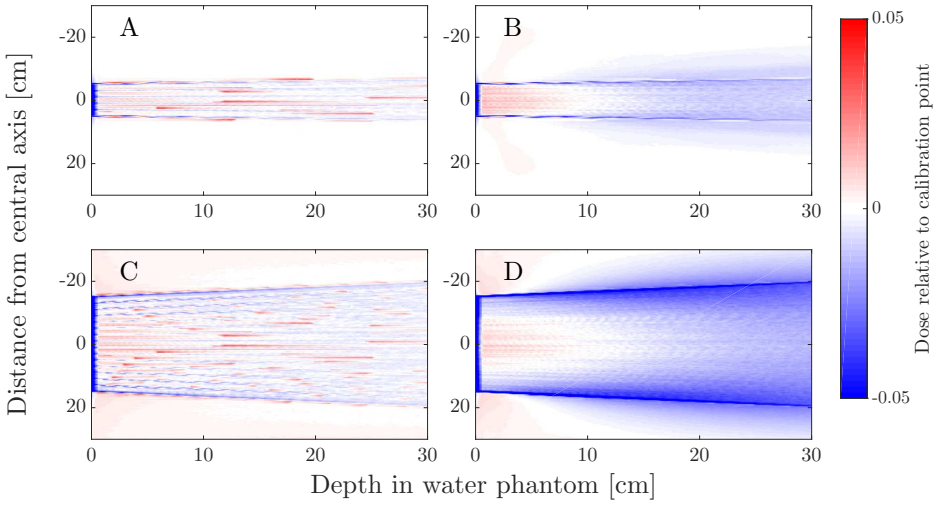

Figure 4.7: Simulations with the simplified machine in the water phantom. Showing the difference in dose between the multi-field model, CC dose algorithm and MC dose algorithm. Subfigure A and C shows the difference between the multi-field model and MC dose algorithm. Subfigure B and D shows the difference between CC dose algorithm and MC dose algorithm. The results in Subfigure A and B were for a field size of 10 cm × 10 cm and the results in Subfigure C and D were for a field size of 30 cm × 30 cm.

4.1.3 Flattening Filter Energy Spectrum

A realistic machine was used to study the effect that the flattening filter energy fluence had on the dose distribution. Two different energy fluence spectrums for flattening filter were studied. The results showed that the dose in penumbra region was dependent of the flattening filter energy fluence and that the effect seemed to be increased at shallower depths, see Figure 4.8. However, the impact seemed to moderate considering the significant difference between the two energy fluence spectrums studied.

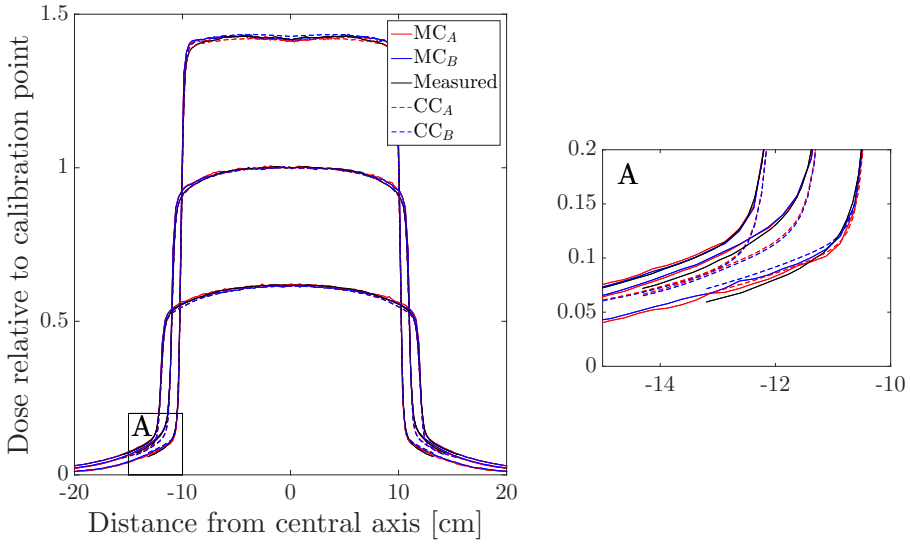

Figure 4.8: Simulations with the flattening filter separation model in the water phantom. Showing the lateral dose at depths of 1.5 cm, 10 cm and 20 cm calculated with the two dose algorithms. The subscripts in the labels indicated the energy fluence spectrum used in the simulation, seen in Figure 3.3. The field size was 20 cm × 20 cm. Subfigure A shows the penumbra region.

4.1.4 New CC Dose Algorithm

The results from the simulation models lead to an implementation of a new CC dose algorithm including a kernel tilt implementation. The dose distribution calculated with the new CC dose algorithm showed an increased resemblance to the MC dose distribution compared to the old CC dose algorithm, see Figures 4.9, 4.10 and 4.11.

Considering the out-of-field dose, the new CC dose algorithm had a dependence on the number of trace directions and seemed to reassemble the MC dose algorithm better for an increased number of trace directions.

Inside the field there was also a dependence on the number of trace directions that seemed more unclear. This can be seen by looking in the area inside the field at the depth of 2.5–5 cm, see Subfigures D and E in Figure 4.11. The behavior of

this area changed with the number of trace directions in an unpredicted manner. This unclear behavior was likely caused by a systematic error in the implementation of new CC dose algorithm.

The perceived large difference in dose at the phantom surface and the field edges was due to the high dose gradients in these regions. Regions with high dose gradients were not fairly represented in these results.

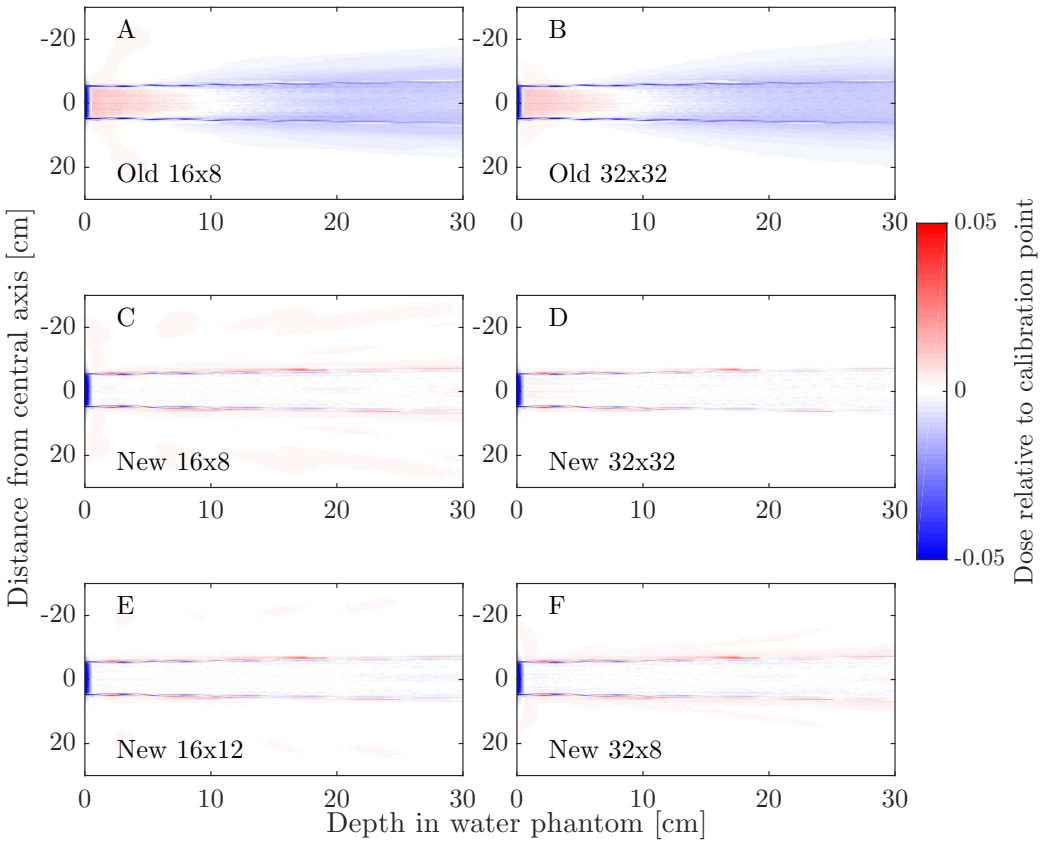

Figure 4.9: Simulations with the simplified machine in the water phantom. Showing the difference between the two CC dose algorithms and the MC dose algorithm. The CC dose algorithm type and number of angular φ bins and θ bins can be seen in each subfigure. The field size was 10 cm $\times$ 10 cm.

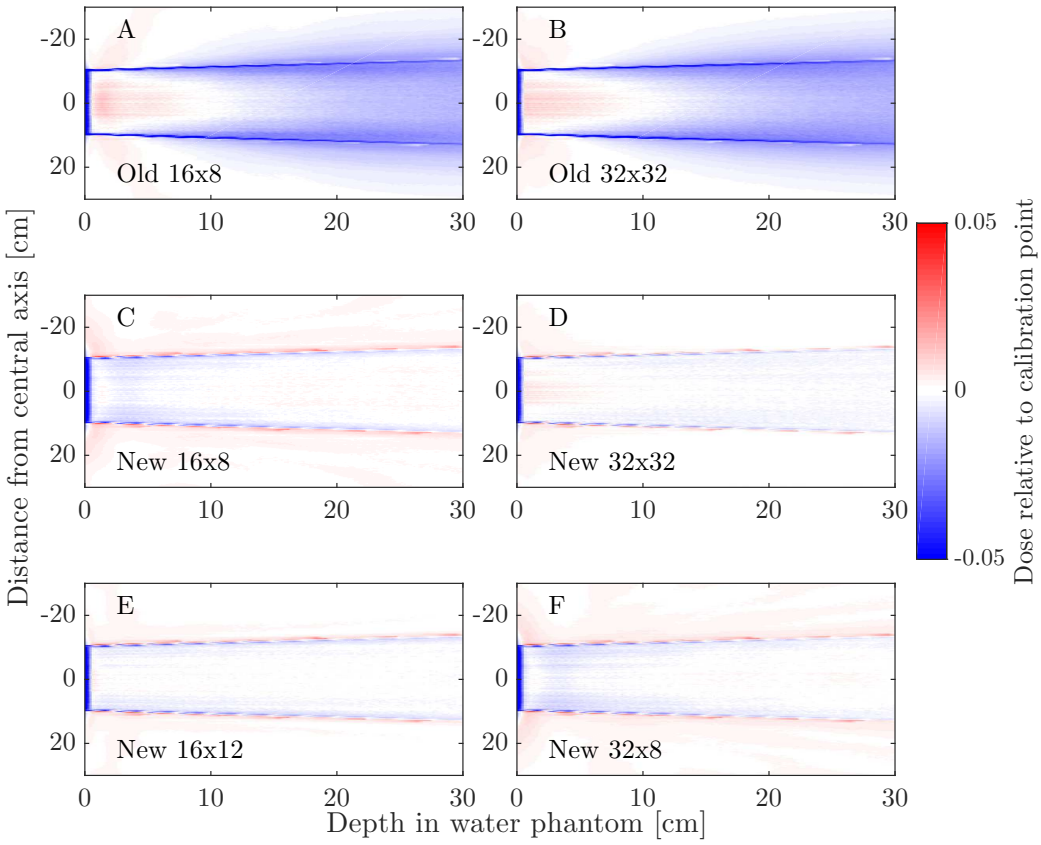

Figure 4.10: Simulations with the simplified machine in the water phantom. Showing the difference between the two CC dose algorithms and the MC dose algorithm. The CC dose algorithm type and number of angular φ bins and θ bins can be seen in each subfigure. The field size was 20 cm $\times$ 20 cm.

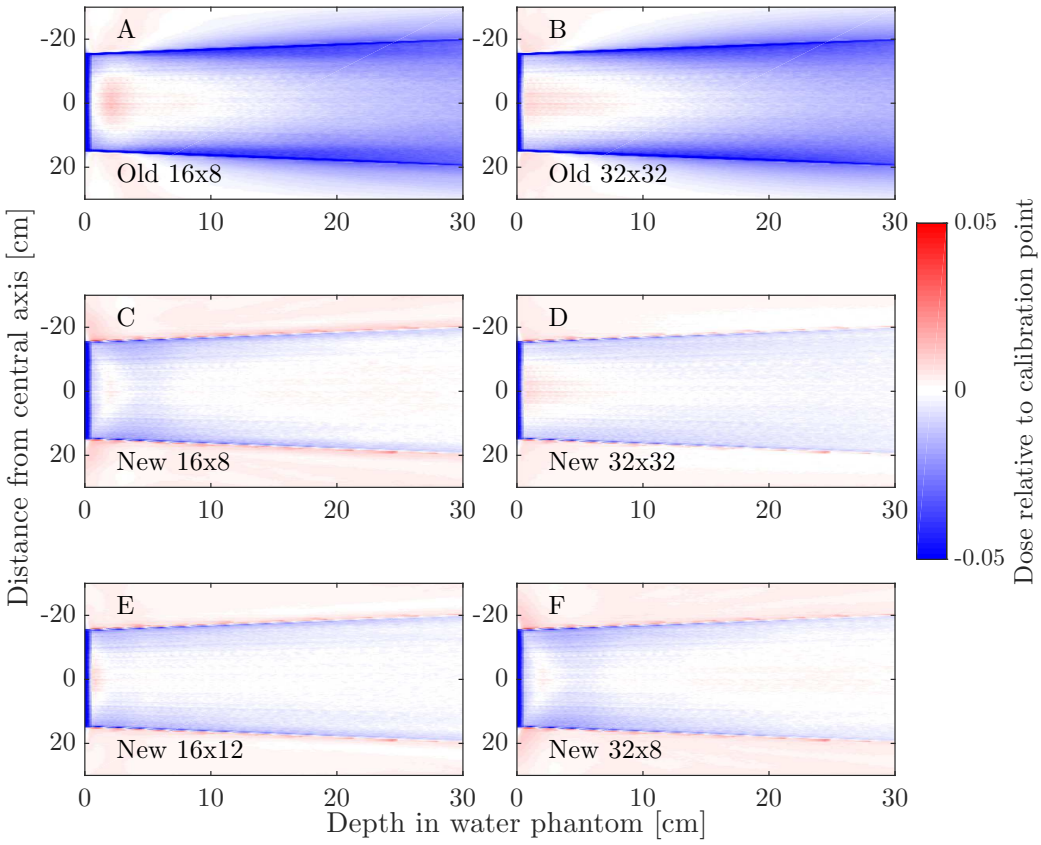

Figure 4.11: Simulations with the simplified machine in the water phantom. Showing the difference between the two CC dose algorithms and the MC dose algorithm. The CC dose algorithm type and number of angular φ bins and θ bins can be seen in each subfigure. The field size was 30 cm $\times$ 30 cm.

The seemingly good agreement between the new CC dose algorithm and the MC dose algorithm was reflected in the scoring of the dose distributions, see Figures 4.12, 4.13 and 4.14.

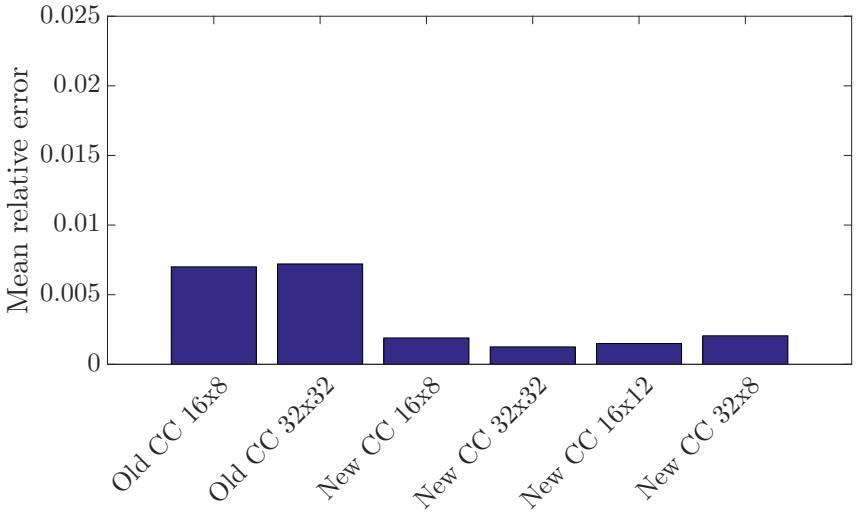

Figure 4.12: The mean relative error between different CC dose algorithms and the MC dose algorithm given by Equation 3.2. The field size was 10 cm × 10 cm.

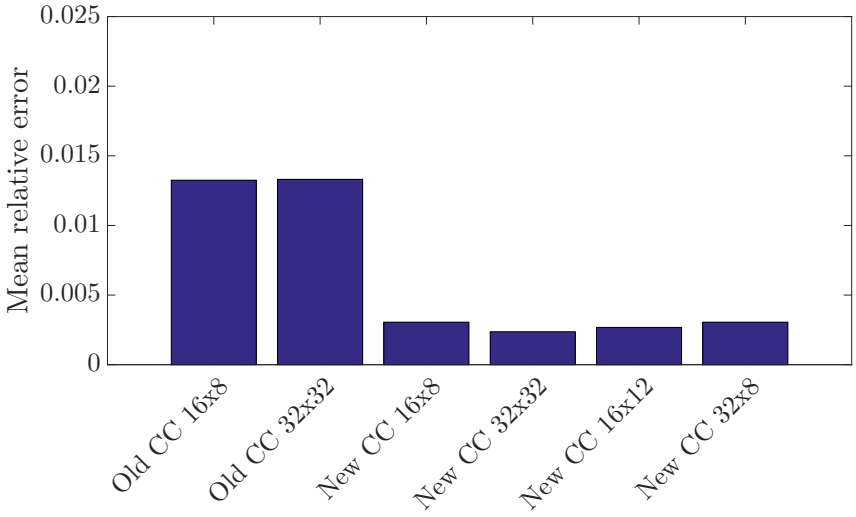

Figure 4.13: The mean relative error between different CC dose algorithms and the MC dose algorithm given by Equation 3.2. The field size was 20 cm × 20 cm.

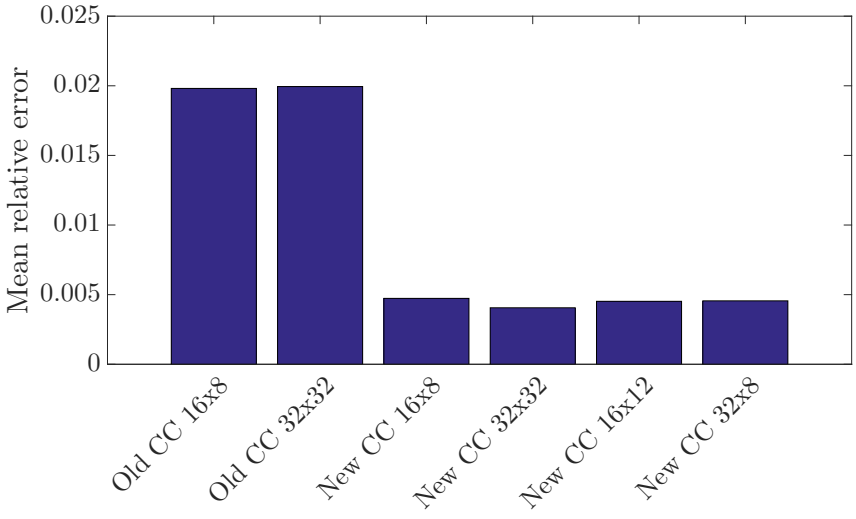

Figure 4.14: The mean relative error between different CC dose algorithms and the MC dose algorithm given by Equation 3.2. The field size was 30 cm $\times$ 30 cm.

The new CC dose algorithm had a lower mean relative error compared to the old CC dose algorithm for all the field sizes. The mean relative error was increased for large fields. The mean relative error seemed to have a marginal dependence on the number of trace directions. However, the score function did not reflect the entire dose distribution since it consisted of selected sample volumes.

4.2 Results from the Heterogeneous Phantoms

The results from the simulations in the first heterogeneous phantom showed that the CC dose algorithm underestimated the dose in bone tissue and overestimated the dose in air, see Figure 4.15. The results confirmed previous results from simulations of a Pinnacle CC dose algorithm done by H Jung *et al.* [7]. The dependence on the number of trace directions was quite small. Furthermore, the difference in scoring dose as dose-to-water or adjusting to dose-to-water from dose-to-medium also seemed to be small.

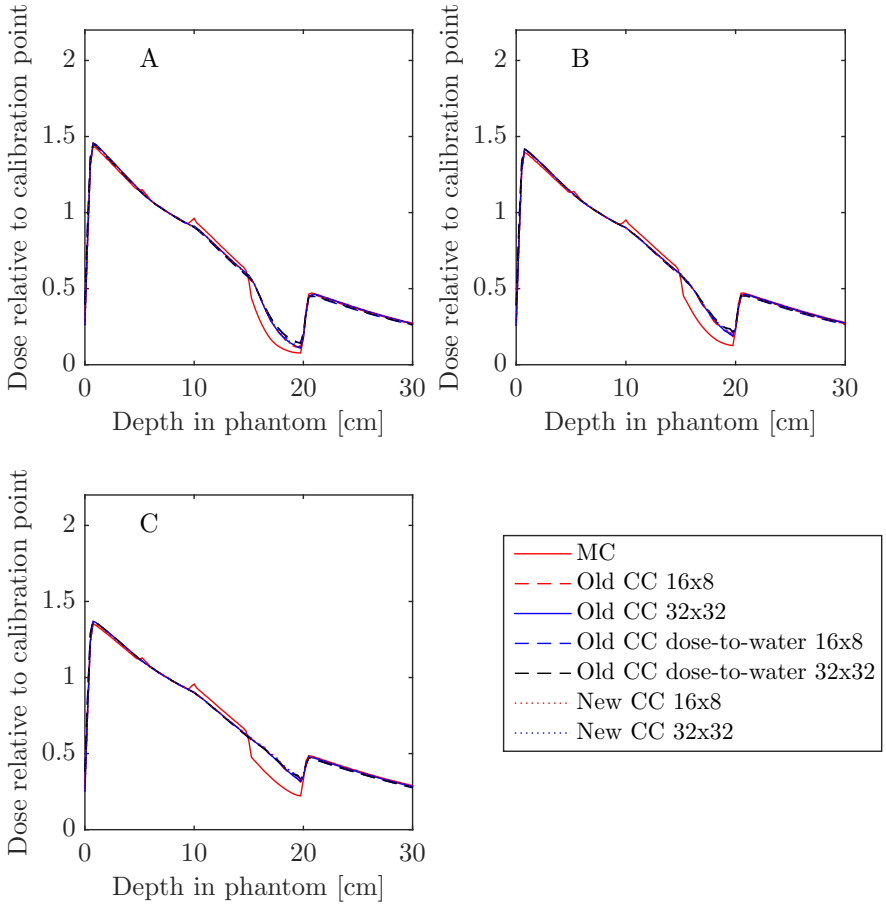

Figure 4.15: Simulations with the simplified machine in the first heterogeneous phantom. Showing the depth dose on the central beam axis. The dose was calculated with the old CC dose algorithm, the new CC dose algorithm and the MC dose algorithm. Two simulations with the old CC dose algorithm calculated dose-to-water. Subfigure A, B and C shows the results for the field size of 2 cm × 2 cm, 3 cm × 3 cm and 5 cm × 5 cm respectively.

The results from the simulations in the second heterogeneous phantom showed that the CC dose algorithm transports less dose out from the field than the MC dose algorithm in low-density regions. As a result, the CC dose algorithm overestimated the dose inside the field and underestimated the dose outside the field compared to the MC dose algorithm, see Figures 4.16 and 4.17.

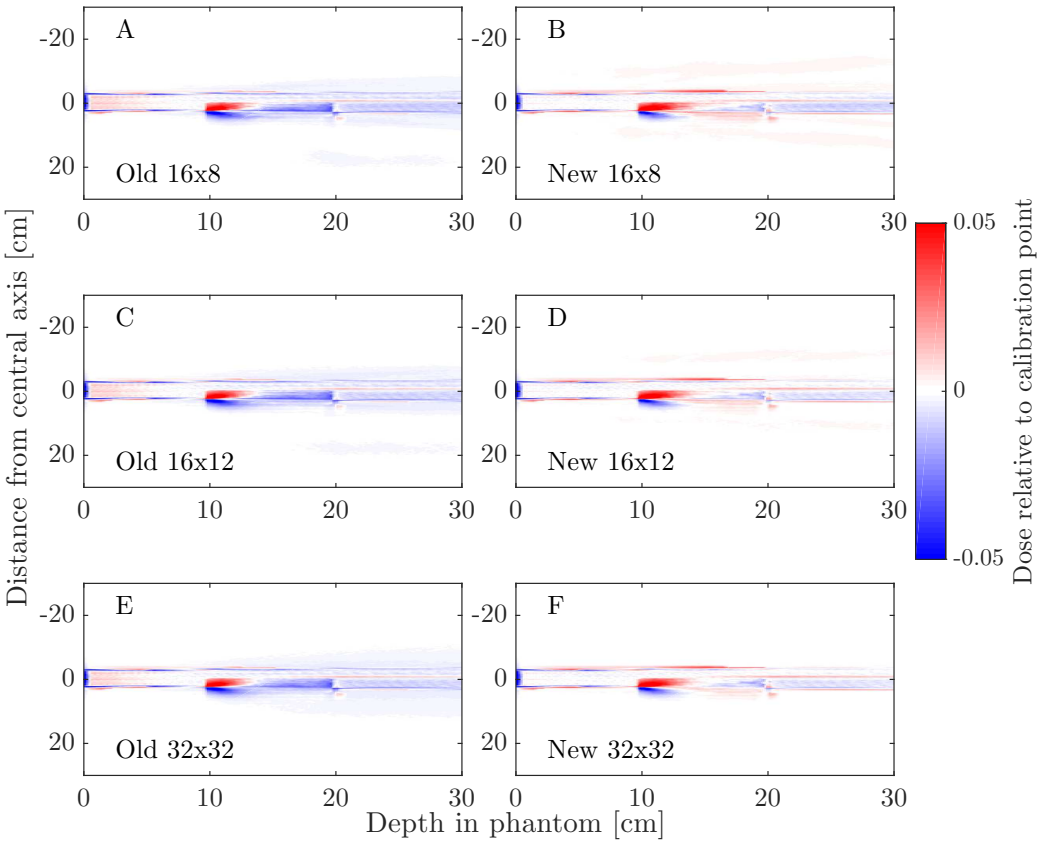

Figure 4.16: Simulations with the simplified machine in the second heterogeneous phantom. Showing differences between the two CC dose algorithms and the MC dose algorithm. The CC dose algorithm type and number of angular φ bins and θ bins can be seen in each subfigure. The density of the lung slab was 0.1 g/cm^3 and the field size was 5 cm $\times$ 5 cm.

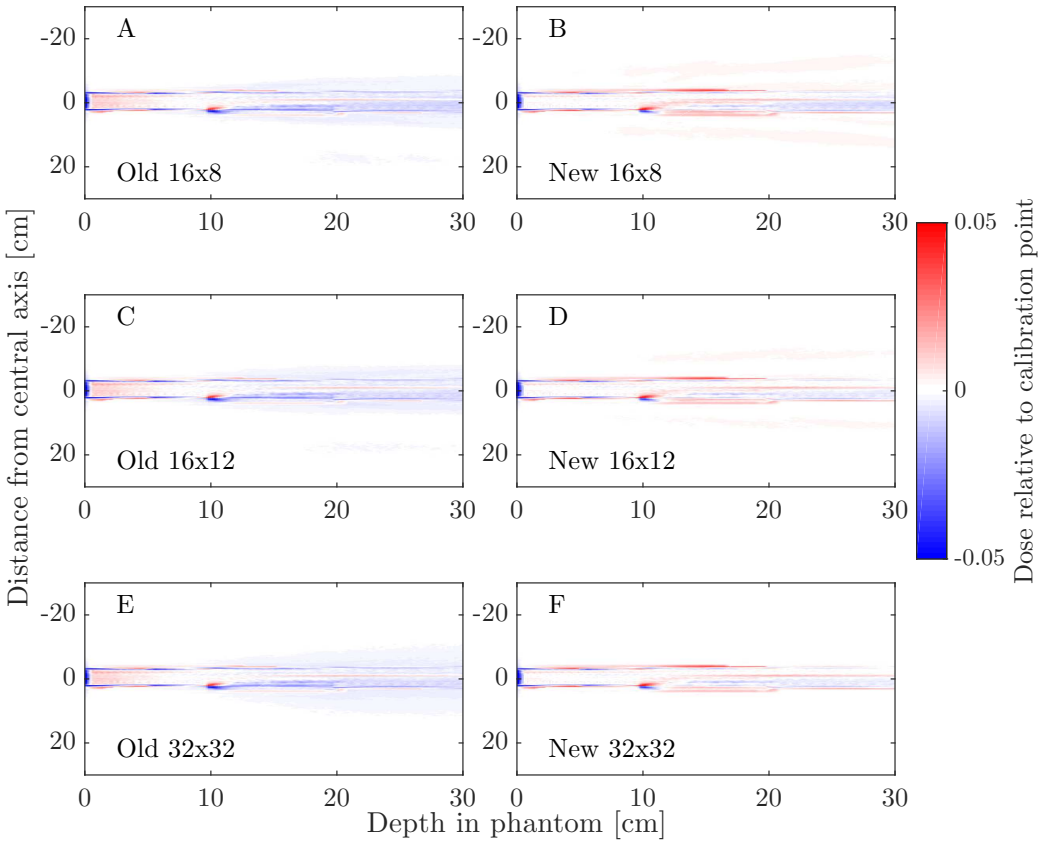

Figure 4.17: Simulations with the simplified machine in the second heterogeneous phantom. Showing differences between the two CC dose algorithms and the MC dose algorithm. The CC dose algorithm type and number of angular φ bins and θ bins can be seen in each subfigure. The density of the lung slab was 0.24 g/cm^3 and the field size was 5 cm $\times$ 5 cm.

The effect was increased for decreased lung densities. The result confirmed previous results by M.K Woo and J.R Cunningham [16]. The discrepancies between the two dose algorithms were due to increased lateral scattering of electrons in low-density regions not predicted by the CC dose algorithm. The effect was visible in areas with lateral charged particle disequilibrium. Moreover, the CC dose algorithm did not account for increased or decreased amount of backscatter in density shifts since the kernels were calculated in water [16].

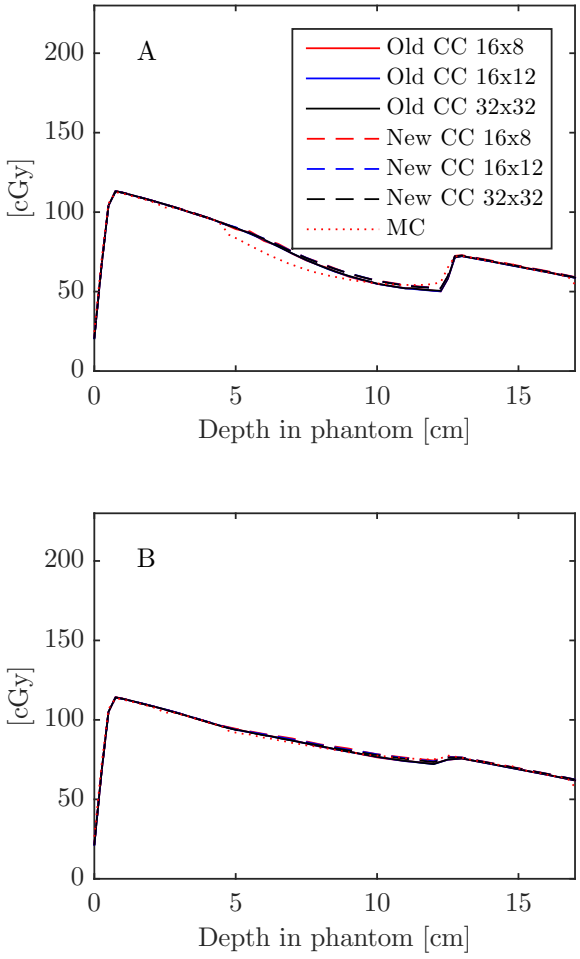

Figure 4.18: Simulations with the simplified machine in the third heterogeneous phantom. Showing the depth dose calculated with the old CC dose algorithm, the new CC dose algorithm and the MC dose algorithm. The dose was calculated with different angular θ bins and angular φ bins. Subfigure A and B shows the result for a field size of 5 cm $\times$ 5 cm field and 10 cm $\times$ 10 cm respectively.

The results from the simulations in the third heterogeneous phantom showed similar tendencies as the previous results, see Figure 4.18. The CC dose algorithm overestimated the in-field dose due to approximations in secondary transport of electrons. The results confirmed previous results by Y.M Guan *et al.* from simulations of a Philips Pinnacle CC dose algorithm [6]. The differences between the CC dose algorithms and the MC dose algorithm seemed be decreased with increasing field size, see the difference between Subfigure A and B in Figure 4.18. This was expected since the effect of lateral charged particle disequilibrium was decreased for larger fields.

Chapter 5

Proposal for Future Work

5.1 Prioritized Improvements

The results from the simulations in the water phantom implied that the differences in dose between the CC dose algorithm and the MC dose algorithm were caused by the no kernel tilt approximation. The energy fluence spectrum of the flattening filter affected the dose in the penumbra region for large fields, however moderately. It is therefore suggested to focus on implementation of kernel tilt in the new CC dose algorithm rather than introducing a new parameter for the flattening filter energy fluence spectrum.

As for the simulations in the heterogeneous phantoms, the CC dose algorithm overestimated the dose in low-density regions compared to the MC dose algorithm. However, the results were generated in extreme cases of inhomogeneities. Nevertheless, it may be seen as an important reminder that the CC dose algorithm has approximations.

5.2 Considerations for Future Implementation

The results from the simulations in water showed increased similarities in dose between the new CC dose algorithm and the MC dose algorithm compared to the old CC dose algorithm. Considering the out-of-field dose, the resemblance between new CC dose algorithm and the MC dose algorithm was better with more θ trace directions, suggesting an increase in the number of θ trace directions from eight to twelve. However, this leads to an increased calculation time in the order of 50%. Moreover, the implementation of kernel tilt alone leads to an increased calculation time. As a consequence, there was a trade-off between the kernel tilt implementation and the complexity of the algorithm. This needs to be taken into account in the event of a new product version of the CC dose algorithm.

Moreover, there seemed to be a systematic error in the implementation of the new CC dose algorithm. The reason for the systematic error might be the collapsing

of the kernel. It was still the unclear how the collapsing and interpolation of the kernel in the new CC dose algorithm should be. This needs to be further evaluated.

Chapter 6

Conclusion

The result from the study in the water phantom showed significant differences in dose calculated with the CC dose algorithm and the MC dose algorithm. The differences were more pronounced for large fields both outside and inside the field. Several simulation models implied the underlying cause of these differences to be the no kernel tilt approximation. The new CC dose algorithm with a kernel tilt implementation showed a four times better agreement with MC dose algorithm compared to the old CC dose algorithm. The flattening filter energy fluence spectrum affected the dose in the penumbra region moderately. The results from the studies in heterogeneous phantoms showed that the CC dose algorithm overestimated the dose in low-density regions compared to the MC dose algorithm. This was due to increased lateral scattering of electrons in low-density regions not predicted by the CC dose algorithm. It was suggested to further develop the new CC dose algorithm to correctly include kernel tilt in the event of a new product version of the CC dose algorithm.

Bibliography

[1] A Ahnesjö. Collapsed cone convolution of radiant energy for photon dose calculation in heterogeneous media. *Medical physics*, 16(4):577–592, 1989.

[2] A Ahnesjö and M.M Aspradakis. Dose calculations for external photon beams in radiotherapy. *Physics in Medicine and Biology*, 44(11):R99, 1999.

[3] Socialstryelsen Cancerfonden. Cancer i siffror. 2013.

[4] I.J Chetty, B Curran, J.E Cygler, J.J DeMarco, G Ezzell, B.A Faddegon, I Kawrakow, P.J Keall, H Liu, C.M Ma, D.W Rogers, J Seuntjens, D Sheikh-Bagheri, and J.V Siebers. Report of the AAPM task group no. 105: Issues associated with clinical implementation of monte carlo-based photon and electron external beam treatment planning. *Medical physics*, 34(12):4818–4853, 2007.

[5] A Einstein. Über einen die erzeugung und verwandlung des lichtes betreffenden heuristischen gesichtspunkt. *Annalen der Physik*, 17(6):132–148, 1905.

[6] Y.M Guan, L.H Zhou, X Zhen, W.T Lu, and S.X Zhang. *Dosimetric verification of collapsed cone convolution algorithm in heterogeneous media.*

[7] H Jung, O Kum, Y Han, B Park, and K.H Cheong. Photon beam dosimetry with EBT3 film in heterogeneous regions: Application to the evaluation of dose-calculation algorithms. *Journal of the Korean Physical Society*, 65(11):1829–1838, 2014.

[8] I Kawrakow. VMC++, electron and photon monte carlo calculations optimized for radiation treatment planning. pages 229–236. 2001.

[9] I Kawrakow and D Rogers. Accurate condensed history monte carlo simulation of electron transport. i. EGSnrc, the new EGS4 version. *Medical physics*, 27(3):485–498, 2000.

[10] C.M Ma and L Jinsheng. Dose specification for radiation therapy: dose to water or dose to medium? *Physics in Medicine and Biology*, 56(10):3073, 2011.

[11] P Mayles, A Nahum, and J.C Rosenwald. *Handbook of Radiotherapy Physics: Theory and Practice.* CRC Press, 2007.

[12] N Papanikolaou, T.R Mackie, C Meger-Wells, M Gehring, and P Reckwerdt. Investigation of the convolution method for poly energetic spectra. *Medical Physics*, 20(5):1327–1336, 1993.

[13] E.B Podgorsak. Review of radiation oncology physics: a handbook for teachers and students. *Vienna, International Atomic Energy Agency. Educational reports series*, 2003.

[14] J Seco and M Evans. Assessing the effect of electron density in photon dose calculations. *Medical physics*, 2000 (Erratum in Med. Phys. 34 (2007) 3121).

[15] J.V Siebers, P.J Keall, A.E Nahum, and R Mohan. Converting absorbed dose to medium to absorbed dose to water for monte carlo based photon beam dose calculations. *Physics in Medicine and Biology*, 45(4):983, 2000.

[16] M.K Woo and J.R Cunningham. The validity of the density scaling method in primary electron transport for photon and electron beams. *Medical physics*, 17(2):187–194, 1990.